Determination of H Adsorption Sites on Pt/C Electrodes in HClO₄ from Pt L₂₃ X-ray Absorption Spectroscopy

M. Teliska,[†] W. E. O'Grady,[‡] and D. E. Ramaker*,[†]

Chemistry Department, George Washington University, Washington, D.C. 20052, and Chemistry Division, Naval Research Laboratory, Washington, D.C. 20375

The adsorption of atomic hydrogen on a platinum electrode in 0.1 M HClO₄ electrolyte was studied in situ with Pt L₂,₃ X-ray absorption spectroscopy (XAS). The Pt electrode was formed of highly dispersed 1.5−2.0-nm particles supported on carbon, and the Pt X-ray absorption fine structure data were collected at room temperature in transmission mode. A novel difference procedure utilizing the L₃ spectra at different applied voltages was used to isolate the effects of H adsorption on the Pt electrode in the XAS spectra. The results obtained in this work are compared with similar results recently reported for H/Pt in the gas phase and with results obtained from real-space full-multiple-scattering calculations utilizing the FEFF8 code on model clusters. The data reveal a number of important points that are similar to those found in the gas phase: (1) at low coverage the H is highly mobile and possibly delocalized on the surface, (2) at higher coverage it localizes into fcc sites, and (3) at very high coverage H is also found in atop sites presumably at or near edges. Point 3 is consistent with that found from previously reported spectroscopic data for Pt/C electrodes. Finally, a detailed interpretation of previously reported electrochemically modulated IR spectra, supporting the XAS analysis, suggests that the delocalized H exists at low coverage and has a profound affect on the water double layer.

Introduction

Hydrogen adsorption on Pt electrodes is regarded as one of the most important systems in electrochemistry. This system has critical applications in fuel cells, water electrolysis, embrittlement, various corrosion processes, and a number of electrocatalyic organic reductions. Studies have shown that adsorbed hydrogen exhibits a strong dependence on factors such as surface-crystallographic orientation and electrolyte composition.[1−4]

Gas-phase studies of H adsorption on metal surfaces have revealed a variety of phenomena, including localization on particular binding sites with thermally activated hopping or even incoherent tunneling between sites to extended band states, depending on the metal, the face, the coverage, temperature, and other adsorbed species.[5−10] Within the last few years, several papers have been published on the nature of the delocalized H, or the quantum mechanical hopping of H from fcc to hcp (face-centered cubic to hexagonal close pack), at low coverage.[11−14]

An extensive review[15] of the literature spanning hundreds of papers over the years, as well as recent papers,[16] reveals that considerable progress has been made in our understanding of H adsorption and the site symmetries on metal surfaces in the gas phase; however, a surprising lack of similar information exists in aqueous environments. This lack of information in the aqueous environment exists even for H adsorption on the most studied Pt(111) single-crystal electrode. Although Raman spectroscopy has confirmed a minor component of H adsorbed in the atop position on polycrystalline Pt occurring at potentials below 0.1 V (relative to the reversible hydrogen electrode,

RHE),[1,17] we are not aware of a single similar spectroscopic report confirming the adsorption site for the majority of the adsorbed H, i.e., the H responsible for the major peak around 0.15 V RHE in the well-known cyclic voltammetry (CV) profiles. Much of the H responsible for the 0.25 V RHE peak is associated with H adsorption at defect and edge sites.[18,19] How does this H adsorption site near edges differ from the major H adsorption site? Do the adsorption sites in aqueous electrolyte change with coverage similar to those in the gas phase? Finally, does delocalized H exist in an aqueous environment? These questions will be addressed in this work. The influence of directly adsorbed anions from the electrolyte on the H adsorption will be discussed elsewhere.[20]

One of the most useful techniques for studying H adsorption in the gas phase is temperature programmed desorption (TPD). It provides bond-strength information (at least the relative isoteric bond strength) for each different binding configuration.[21] The standard CV curve in electrochemistry provides comparable information, since the potential is directly related to the Gibbs free energy of adsorption (ΔG).[22,23] However, while up to 6 different features are seen in the H TPD curves for polycrystalline Pt, normally only 2−4 features are seen in the CV curves. Since both the potential and temperature can be varied in electrochemistry, both the ΔH and ΔS values for adsorption of H in the primary two absorption sites found for H/Pt in an electrochemical environment have been obtained from the CV curves. Further, the ΔH values obtained from these studies are comparable to those obtained in the gas phase and from theoretical calculations,[24] suggesting strongly that the H binding sites in the electrolyte and gas phase are comparable.

The lack of direct H binding site information in an electrochemical cell arises in part because the various vibrational spectroscopies used in the gas phase (to be summarized below)

* To whom correspondence should be addressed. Tel: 202-994-6934. Fax: 202-994-5873. E-mail:ramaker@gwu.edu.
† George Washington University.
‡ Naval Research Laboratory.

cannot be used with similar success in an aqueous environment. This is due to the huge absorption of IR and other wavelength radiation by the bulk water. Over the past two decades, several techniques have been developed to avoid this absorption or at least cancel it out. These techniques involve difference or differential techniques, such as electrochemically modulated infrared spectra, EMIRS,[25,26] or second harmonic generation, SHG,[27-29] but these techniques have not been as successful as the normal vibrational techniques utilized in the gas phase. Furthermore, the Pt electrode, sometimes a single crystal (SC), more often polycrystalline or supported Pt clusters, is usually not as well characterized compared to the Pt surfaces used in the gas phase. Finally in aqueous electrolytes, H-bonded water in the double layer and directly adsorbed anions such as bisulfate can even further complicate the H adsorption process.[30-33]

As indicated, the primary reason for the lack of detailed information on H adsorption in an electrochemical cell is the absence of a general in situ spectroscopic technique that can provide site symmetry information. X-ray absorption spectroscopy (XAS) is one spectroscopic technique that can be applied in situ because XAS is one of only a few probes that utilizes X-rays exclusively (i.e., X-rays in and X-rays out, when using transmission or fluorescence yield mode),[34] and the latter are not significantly absorbed by the bulk water in the energy region of the Pt L_{23} edge, such as in the IR region. However, XAS has been limited until recently to providing geometric information on systems with short-range order (via extended X-ray absorption fine structure (EXAFS)) and to "scatterers" generally much larger than H. The stimulus for this work is recent advances in XAS (in both XAFS and X-ray absorption near edge structure, XANES), which now enable XAS to provide H binding site information.

These recent advances arise from new data analysis procedures rather than new experimental techniques. Procedures for quantitatively isolating the "atomic" XAFS (AXAFS) structure in the XAFS data have been recently reported.[35-40] Although this will not be used in this work, we have shown that this structure can provide direct information about the surface charge on an electrode in situ[41] and the nature of the polarization across a cation–anion pair in an electrolyte.[42] It has recently been suggested that isolation of the Pt–H scattering in the XANES data can provide direct information about the nature of the Pt–H binding site.[43] Here, this Pt–H scattering technique will be applied for the first time in situ to an aqueous electrochemical cell, where the H adsorption comes from proton reduction. This work will expand on the recent theoretical results of Ankudinov et al. using the FEFF8 code[44] to confirm that this technique can indeed provide direct information on the H adsorption site. Finally, evidence for delocalized H at low coverage will be discussed utilizing previously published EMIRS data[26,45] and the new XANES results reported here.

XANES data has been utilized previously to examine the effects of Pt–H bonding.[46,47] In a study of carbon-supported Pt electrodes by Mukerjee and McBreen,[48] an increase in the white-line area was observed in the potential region where H is electrochemically adsorbed. Increases or other changes in the white-line areas have also been observed after gas-phase adsorption of H_2 by a number of workers.[49-52] Mansour and Sayers[53] attributed the changes in the white-line areas to changes in the occupancy of the d orbitals at the Fermi level and developed a quantitative technique for determining the number of unoccupied d-electron states. It will be shown here that most of the changes result directly from the Pt–H scattering and these effects can be isolated.

Experimental Section

A. Sample Preparation. For the in situ XAS experiments, Teflon-bonded Pt/C electrodes were fabricated using the following procedure.[54] A 0.6 g sample of 10 wt % Pt/C is mixed with 0.1 g of chopped carbon fiber in a 150-mL beaker. To this mixture is added 5 mL of water containing a sufficient amount of Dupont T-30 Teflon suspension to make the Pt/C and carbon fiber mixture 10 to 12 wt % Teflon. This mixture is sonicated for 1 min, then 100 mL of water is added to the mixture in 25-mL steps each followed by sonication for 1 min. Following the final sonication, the mixture is evacuated through filter paper on a vacuum table making a 5 cm diameter sample. The evacuated sample is removed from the filter paper, dried at 75 °C, and then sintered at 320 °C under nitrogen or argon for 10 min.

The cell used in these measurements was similar to that described previously.[54] The Pt/C electrode was flooded with 0.1 M $HClO_4$ and held in a PTFE gasket. The counterelectrode was an uncatalyzed high-surface-area carbon electrode flooded with the same electrolyte as the Pt electrode and held in a PTFE gasket. Nafion or filter paper, saturated with the same electrolyte, were used as separators. The reference electrode was a Pd/H electrode, and all the data are reported relative to the RHE. The potential in the cell was controlled with a PARC 273 potentiostat. The Pt L_3 data was recorded in 0.1 M $HClO_4$ at 0.0, 0.1, 0.2, 0.3, 0.54, 0.8, and 1.14 V vs RHE. The Pt electrode is reduced electrochemically after fabrication by holding the electrode at 0.0 V (RHE) for an extended period.

B. X-ray Absorption Experiments. The Pt XAFS data were collected at room temperature in transmission mode on beamline X-11A of the National Synchrotron Light Source (NSLS) at Brookhaven National Laboratory. The NSLS storage ring operated at 2.52 GeV beam energy with ring currents between 40 and 200 mA. Three gas-flow ionization detectors were used to monitor the intensities of the incident (I_0) and transmitted X-rays (I) through the sample and the reference detector (I_{ref}). The Si(111) double-crystal monochromator was detuned by 30% at 200 eV above the Pt L_3 edge (11 564 eV) to minimize the presence of higher harmonics in the beam. The energy calibration was achieved by recording the XAFS of a 7 μm thick Pt foil simultaneously with the sample.

Theoretical

A. EXAFS and XANES Analysis. The EXAFS analysis was performed using the WINXAS code.[55] The pre-edge background was removed using a linear polynomial, and the many-body S_o^2 factor fixed at 0.934 was calculated with the FEFF8 code. The postedge background was removed using the usual spline technique and smoothing criteria that leave the atomic XAFS in the χ function as described previously.[35-39] Reference phase and amplitude functions for the Pt–Pt scattering were obtained from FEFF8 calculations on a Pt_6 cluster.

The original analysis procedure for isolation of the H scattering contribution in the XANES data has been previously published.[56-60] A brief summary is given here since significant modifications have been made to the original method.

The absorption coefficient, μ, is given as $\mu_o(1 + \chi)$. The contribution of the adsorbed H to μ is obtained by subtracting out the μ data of the reference spectrum from the μ data containing the H contribution so the total change in the difference spectrum, $\Delta\mu = \mu(H/Pt) - \mu(Pt)$ is isolated. This can further be expressed as

$$\Delta\mu = \Delta\mu_o + \Delta[\mu_o\chi_{Pt-Pt}] + \mu_{o,H}\chi_{Pt-H} \qquad (1)$$

H Adsorption Sites on Pt/C Electrodes

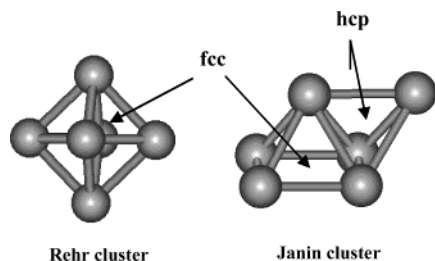*J. Phys. Chem. B, Vol. 108, No. 7, 2004* **2335**

Figure 1. Illustration of octahedral Pt_6 cluster used by Ankudinov et al.[44] (left) and that used by Janin et al.[64] (right). The fcc and hcp sites are also indicated on the "Janin" cluster. All fcc sites are the same on the octahedral site.

These 3 terms include the H-induced changes in the AXAFS ($\Delta\mu_o = \mu_{o,H} - \mu_{o,ref}$). The second term reflects the changes in the Pt−Pt scattering, $\Delta(\mu_o\chi_{Pt-Pt})$, which exhibits the largest change with adsorption site symmetry and allows us to determine the absorption sites. The third term is the Pt−H scattering ($\mu_{o,H}\chi_{Pt-H}$) arising from the H adsorption.

The experimental difference spectra, $\Delta\mu = \mu(H/Pt) - \mu(Pt)$, were obtained by subtracting the L_3 edge spectrum recorded at 0.54 V from the L_3 edge spectra recorded at the potentials in the hydrogen region of the voltammogram. At 0.54 V, the Pt electrode lies in the double-layer region where there is no adsorbed hydrogen or adsorbed ClO_4^- anion. The spectra were aligned before subtraction by aligning the Pt foil reference spectra and then shifting the sample spectra according to the foil data.

B. FEFF Calculations. FEFF8 calculations[61] were performed to interpret the $\Delta\mu$ spectra using a series of Pt_6 and Pt_6H_x clusters as illustrated in Figure 1 and in the figures below.

The octahedral cluster on the left in Figure 1 was utilized previously by Ankudinov et al.[44,62,63] to model H adsorption in 3-fold fcc sites. In contrast, Janin et al.[64] preferred the cluster on the right because it contains both fcc and hcp sites as indicated. The "Janin" cluster also has considerably lower symmetry than the octahedral cluster on the left. This has the advantage that a surface state near the Fermi level does not arise, a surface state that is unique to the symmetric octahedral Pt_6 case. This surface resonance has been shown to produce a peak in the unoccupied density of states (DOS) just above the Fermi level, which is very detrimental to the accurate prediction of the general $\Delta\mu$ signatures by FEFF8 as discussed previously.[44] Thus throughout this work, the "Janin" Pt_6 cluster is utilized, with the Pt−Pt distance at 2.77 Å and the Pt−H distance at 1.8 Å.

It is known that with the FEFF8 code, the results are highly dependent on the potentials used in the code. Previously it was found that the Dirac−Hara potential with an imaginary part of 5 eV was optimal for describing the Pt−Pt and Pt−O scattering.[35,37] However, the emphasis in that optimization procedure was placed on the 25−150-eV region. Here the region below 40 eV is of interest. Although a more complete analysis in this energy region is required, the Hedin−Lundquist potential is preferred and used in this work to describe the Pt−H scattering following the work of Ankudinov et al.[62,63]

XANES is dominated by multiple scattering particularly near the edge. Thus both χ_{Pt-Pt} and χ_{Pt-H} must include both the single and the multiple scattering contributions. In this study, the Pt−Pt scattering has to be separated from the Pt−H scattering in order to give the separate contributions. This was accomplished by performing full multiple scattering (FMS) calculations with different FMS radii around the absorbing atom (full scattering is included from atoms only within the FMS radius). To isolate
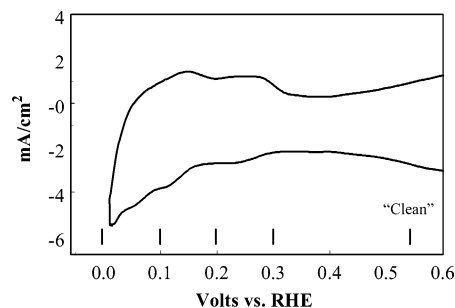

Figure 2. Figure 2. Current vs potential (V vs RHE) in the hydrogen region for a Pt electrode in 0.1 M $HClO_4$. The potentials where the XANES data were taken are also indicated, and the voltage at 0.54 V RHE, which is used as the reference or the "clean" electrode, is highlighted.

TABLE 1: Summary of EXAFS First-Shell Pt−Pt Fit Results[a]

potential (V, RHE)	N [$\Delta N = 0.3$[b]]	R (Å) [$\Delta R = 0.02$[b]]	E_o (eV)	σ^2 (Å²)
0.54	8.4	2.74	1.9	0.0073
0.30	8.3	2.74	1.8	0.0072
0.20	8.4	2.74	1.9	0.0073
0.10	8.5	2.75	2.0	0.0067
0.00	8.8	2.76	1.0	0.0067

[a] S_o^2 fixed at 0.934 as calculated by FEFF8. [b] Although the absolute values of ΔN and ΔR are certainly larger than that indicated, the variation in the values of N and R with potential are believed to be meaningful down to the values indicated.

the Pt−H scattering contribution, the FMS radius was set to 2.4 Å, less than the Pt−Pt bond length of 2.77 Å but greater than the Pt−H bond length around 1.8 Å. A second calculation to isolate the Pt−Pt scattering contribution was carried out using a larger FMS radius, 8 Å, which includes all of the scattering elements. To isolate the Pt−H scattering, the difference is taken between these two calculations.

Results

Figure 2 shows the cyclic voltammogram for a Pt/C electrode recorded in 0.1 M $HClO_4$. The potentials where the XAS data were recorded in the $HClO_4$ are indicated in the figure.

Results from the EXAFS analysis of the data taken at each potential are summarized in Table 1. These results reveal that the particles have a coordination number around 8 and therefore have an average particle size of around 1.5−2 μm based on model cluster calculations assuming spherical clusters.[65] Further, these particles show a Pt−Pt distance smaller than in bulk Pt (2.77), consistent with that found previously,[56−60] and relaxation back to a slightly larger Pt−Pt distance as H is adsorbed on the cluster. A small increase in coordination number with H coverage may also be evident, but this increase is near the uncertainty level. Figure 3 shows the Fourier Transform, FT, of the EXAFS data taken at 0.54 and 0.8 V (RHE), the peak at $R = 1.6$ Å demonstrating the presence of O(H) on the surface at 0.8 V. The data at 0.54 V is essentially the same at that in the region 0.1−0.3 V, suggesting that the small feature around $R = 1.5$ Å at 0.54 V is within the background noise level and therefore not due to Pt−O scattering. This suggests that the Pt surface is relatively "clean" as seen by XAFS already at 0.54 V. The XAFS apparently does not "see" the water double layer or any directly absorbed cations such as ClO_4^- (the latter is known not to directly absorb on Pt). The lack of scattering from the double layer presumably arises because it is not sufficiently ordered on the surface to give a significant contribution to the
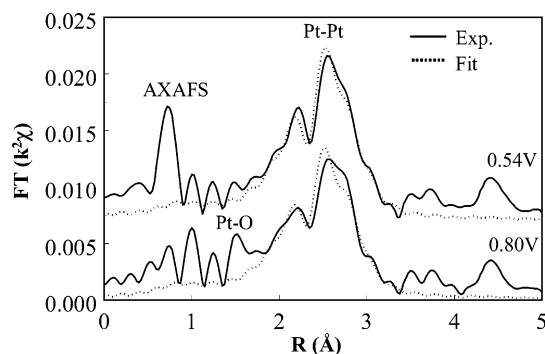
Figure 3. Magnitude of the Fourier Transform of the experimental EXAFS, FT(χ), (k^2, $\Delta k = 1.5 < k < 17$ Å^{-1}) taken at 0.54 and 0.80 V (RHE) (solid lines). Also shown is the first-shell Pt−Pt fit ($\Delta R = 1.34−3$ Å) with theoretical references obtained from FEFF8 calculations on a Pt$_6$ cluster (dotted lines).
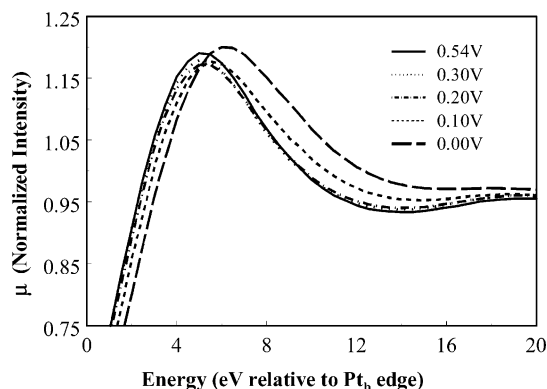

Figure 4. The XANES data (μ) at the potentials indicated, normalized to 1 at 50 eV and on an energy scale relative to the bulk Pt edge. These spectra were carefully energy calibrated but were not otherwise aligned or shifted.
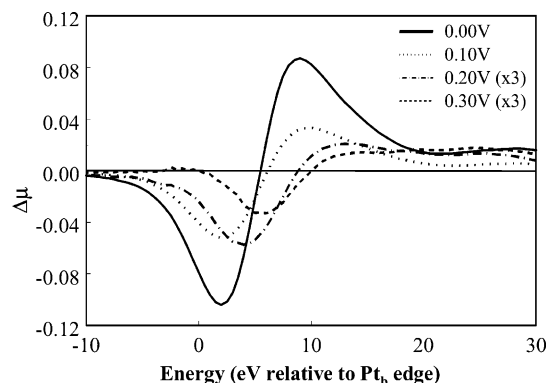

Figure 5. The $\Delta\mu$ difference spectra $\mu(x.x) - \mu(0.54)$, at the indicated $x.x$ potentials. The data for 0.2 and 0.3 V were scaled by a factor of 3 to make them more visible.

EXAFS. The absence of a significant H peak below 0.3 V arises because with the k^2 weighting in the FT the Pt−H scattering is negligible even at high H coverage, although it will be clearly seen in the XANES $\Delta\mu$.

Figure 4 shows the L$_3$ XANES data for a Pt/C electrode at several voltages in 0.1 M HClO$_4$. The L$_3$ edges change significantly with applied potential as the Pt−H bonds are formed or removed from the surface. By taking differences of these L$_3$ spectra at different potentials, we are able to isolate the individual contributions causing these changes. Figure 5 shows the $\Delta\mu$ difference spectra using the 0.54-V spectrum as the reference. A systematic trend is seen in these data; the amplitude and line shape change with increase in the hydrogen coverage.
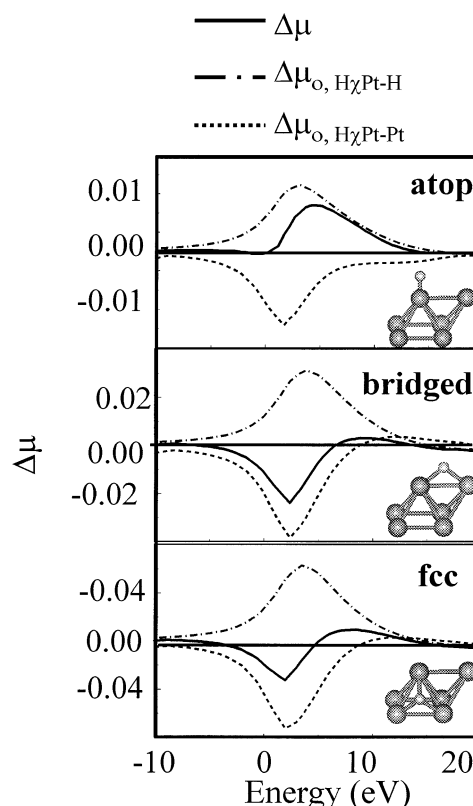

Figure 6. Theoretical $\Delta\mu = \mu(\text{H/Pt}_6) - \mu(\text{Pt})$ difference spectra (heavy solid line) and the two components $\Delta[\mu_o\chi_{\text{Pt−Pt}}]$ (dashed line) and $\mu_{o,H}\chi_{\text{Pt−H}}$ (dot-dashed line) obtained from FEFF8 calculations on the clusters illustrated, with H in the atop, bridged, and 3-fold (fcc) sites. The Pt−H distance was set at 1.8 Å and the Pt−Pt distance at 2.77 Å, and the left-upper Pt atom (i.e., the one closest to the H atom) was taken as the absorber atom in all cases.

Figure 6 shows the FEFF8 results for the cluster models with increasing Pt−H coordination (1 for atop, 2 for bridged, and 3 for the 3-fold fcc). The individual contributions ($\Delta[\mu_o\chi_{\text{Pt−Pt}}]$ and $\mu_{o,H}\chi_{\text{Pt−H}}$) and the total difference $\Delta\mu$ are shown. The $\Delta\mu_o$ term is the smallest of the three terms and is greatly exaggerated by the calculations on such small clusters, so consistent with previous work we ignore this term here.[66] The results in Figure 6 clearly show a dependence of $\Delta\mu$ on the adsorption site. The $\mu_o\chi_{\text{Pt−H}}$ term changes in magnitude but not in spectral shape when the Pt−H coordination changes from 3 in the fcc case to 1 in the atop case. The $\Delta[\mu_o\Delta\chi_{\text{Pt−Pt}}]$ term varies the most dramatically on changing the hydrogen adsorption site.

These changes in $\Delta[\mu_o\chi_{\text{Pt−Pt}}]$ with adsorption site can be related directly to the different bonding at these sites. When H atoms are adsorbed on the fcc site, hydrogen weakens the Pt−Pt bonds with the Pt atoms beneath the hydrogen adsorption site. This bond weakening has been called d-electron frustration by Feibelman[67] and Pt−Pt destabilization by Papoian et al.[68] Recent generalized valence-bond calculations by Kua et al.[24] also revealed that Pt−H coordination in the fcc site results in a weakening of the Pt−Pt bonding beneath the H atom. Figure 6 shows that the $\Delta[\mu_o\chi_{\text{Pt−Pt}}]$ contribution is much smaller when the hydrogen is bonded in the atop position, which allows the Pt−H contribution to dominate. The weakening of the Pt−Pt bonding when H is bonded in the fcc site reduces the Pt DOS just above the Fermi level, making the $\mu_o\Delta\chi_{\text{Pt−Pt}}$ more negative.

The $\Delta\mu$ results for H in the atop, bridged, and fcc sites on the Pt$_6$ cluster are compared and shown in Figure 7. The amplitude of the total $\Delta\mu$ increases in the order atop < bridged < fcc, showing a consistent trend. The differences between $\Delta\mu$
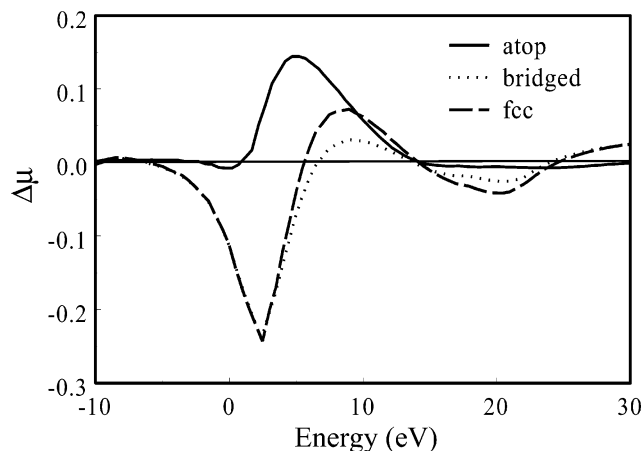
H Adsorption Sites on Pt/C Electrodes

J. Phys. Chem. B, Vol. 108, No. 7, 2004 **2337**

Figure 7. Comparison of the three $\Delta\mu$ spectra from Figure 4, showing the different "signatures" for the atop (1-fold) vs the bridge (2-fold) and fcc (3-fold) coordination sites

Figure 8. Comparison of previously reported TPD data for the different systems indicated. Data for single-crystal Pt(111),[71] single-crystal Pt(335),[19] polycrystalline Pt,[72] and Pt black[9] are shown. The lines at the top indicate the temperature range where atop (light-dotted line), 3-fold (solid line), and delocalized H (dashed line) are being removed. The vertical line separates the temperatures for H desorbing from flat faces vs that from steps.

for the bridged and fcc sites are not significant enough to distinguish between these two sites. Results for the hcp site (not shown) are essentially the same as the fcc site. Therefore, the signature or fingerprint for the atop site is unique, and only this site can be distinguished from the other sites for H/Pt. As indicated above, these theoretical results are sensitive to the Pt–H bond length, potential utilized in FEFF8, and other parameters in the calculations. Therefore, we do not anticipate necessarily quantitative agreement between the theoretical $\Delta\mu$ fingerprints identified here and the experiment, but rather we utilize the theoretical results to identify distinguishing features between the atop vs the higher coordination sites. The atop signature has negligible negative contribution while the bridge/fcc signatures have a large negative contribution. Further discussion of the atop and bridge/fcc line shapes can be found elsewhere.[44,66]

Discussion

A. Hydrogen Adsorption on Pt. Hydrogen adsorption on Pt in the gas phase, as mentioned in the Introduction, has been extensively studied using many techniques. These results will be summarized and discussed here in order to make comparison with results found here in an electrolyte. Although some differences between the gas phase and the electrochemical situation are expected due to interferences in the electrochemical double layer, it will be shown below that these differences are not significant. Hydrogen adsorption on Pt studied by TPD[69] provides a direct measure of the Pt–H bonding energy. Ion-channeling techniques have been utilized which directly reveal the adsorption site.[6,70] These techniques collectively have greatly enhanced knowledge of H adsorption on Pt, but the interpretation of these data has not been without controversy.

TPD data from H/Pt(111) reveals a single broad peak that is sometimes partially resolved into a peak around 300 K with a shoulder at 260 K (see Figure 8). At low coverage, only the high-temperature peak is observed, the shoulder becoming more pronounced with coverage.[71] The introduction of steps on the surface (i.e., a Pt(335) surface) reveals the same features mentioned above, plus additional features around 350 and 380 K and an increased shoulder to lower temperatures around 220 K.[19] TPD data for polycrystalline Pt show essentially the same features.[72] Finally TPD data from Pt black shows the lowest 220 K feature and the highest features around 350 and 380 K but with the middle features around 260 and 300 K now nearly absent (see Figure 8).[9]
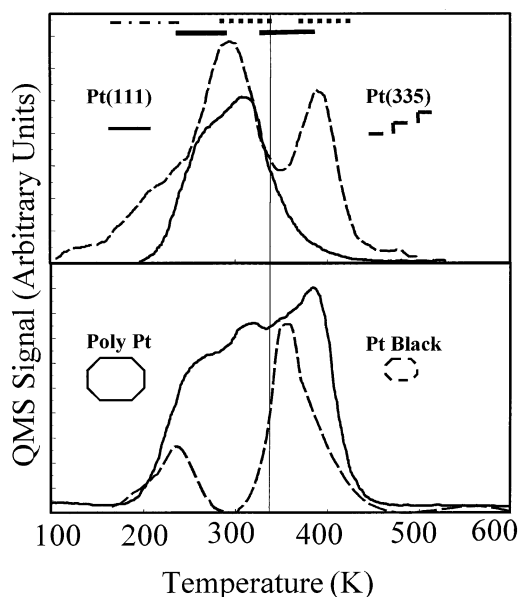
Before the assignment of these three TPD features, it is helpful to examine the vibrational spectroscopy data. The vibrational spectroscopies included high-resolution electron energy loss spectroscopy (HREELS),[73] IR (usually utilizing the so-called SNIFTERS technique[74] but also using the sum frequency generation (SFG) technique),[75,76] Raman,[77,78] and neutron inelastic scattering (NIS).[79] All of these techniques generally reflect the vibrational spectra, but each has its advantages and disadvantages. NIS requires a large amount of sample with high specific area; hence, it has not been utilized for SC samples but rather on Pt black or supported Pt.[79] However NIS has the advantage that all transitions are active so that important excitations that are dipole inactive in the IR still show up in the NIS. The IR techniques have been utilized on both SC and polycrystalline samples, but miss important transitions that are dipole inactive, such as the symmetric and asymmetric stretch modes in the fcc site. HREELS can sample both the dipole-active and -inactive transitions (using the specular and off-specular techniques), but the data is often noisy.

Figure 9 summarizes the important vibrational data for Pt(111)[73] and Pt black[79] or supported Pt particles. Notice the striking similarity of these data. As far as the site symmetries are concerned, the Pt particles are essentially cuboctahedral in shape with (111) flat faces and (100) edges.[80] The assignment of the individual peaks has been controversial. Initially, comparison with IR data from metal complexes was utilized, but more recently, theoretical calculations have been the most helpful. On the basis of these calculations and other data, general agreement has now been reached on these assignments.[19] The peak at 550 cm^{-1} is assigned to delocalized H, i.e., H quantum mechanically delocalized over two adjacent 3-fold sites (fcc–hcp) on a sub-picosecond time or even completely delocalized.[81] This will be further discussed below. The broad peaks at 1000–1500 cm^{-1} are attributed to H localized in the fcc site and the peak around 2030–2090 cm^{-1} to H in the atop site.[82] The latter peak is most visible for Pt clusters at very high coverages of near a monolayer.
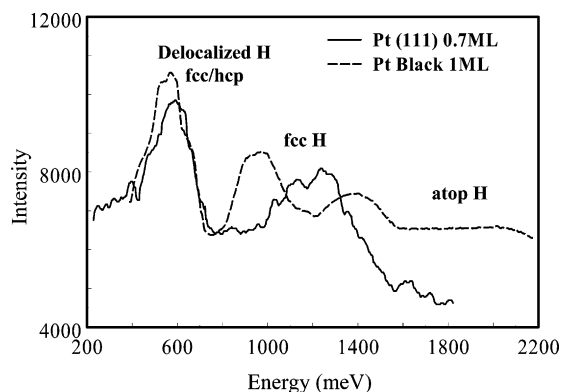
Figure 9. Comparison of previously reported HREELS data for 0.7 ML H/Pt(111)[73] with NIS data[79] for 1 ML H/Pt black. The spectral regions where the delocalized H, fcc H, and atop H contribute are indicated.
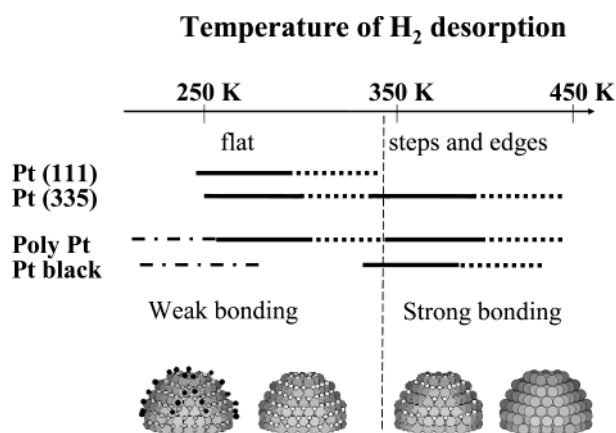

Figure 10. Summary of TPD from Figure 8, showing regions where delocalized (dashed line), 3-fold (solid line), and atop (dot-dashed line) H desorb are shown. The separation between weakly bonded H on the flat faces, and strongly bonded H at the edges is also indicated. Also illustrated are clusters with the adsorbed H expected on the surface in the temperature range immediately above the cluster. Dark atoms are atop, light atoms, 3-fold.

Finally, both the transmission−ion-channeling data[6] and the recoiling or backscattering channeling data[70] indicate that H preferentially populates the fcc sites on Pt(111); however, the H atoms root-mean-square displacement parallel to the surface is quite large. These experiments are usually done at near monolayer coverages, where the adsorption sites are indeed believed to be fcc. We question the coverages reported by Rabalais and co-workers[70] since they report a full 1×1 LEED pattern at 0.2 ML. Most other workers report a LEED pattern only at coverages well beyond 0.6 ML after H localization into the fcc site has set in.[5]

Taking these data together suggest the following interpretations as summarized in Figure 10. The features around 260 and 360 K in the TPD curves are believed to arise from H in 3-fold hollow sites. At low coverages on Pt(111), the 310 K peak arises from the delocalized fcc−hcp adsorbed H. As the coverage increases, the H localizes into the preferred fcc sites, producing the 260 K peak. The presence of defects and edges, which cause the 360 and 390 K TPD peaks, still arise from localized and fcc−hcp-delocalized H, respectively, but now fcc−hcp sites near the defects or edges. H apparently can also adsorb directly on the atop edge sites at saturation coverages producing the lowest shoulder around 150−250 K but not on the flat Pt(111) surfaces.[81] The near absence of the 260 and 310 K features on Pt black apparently occurs because for these small clusters little
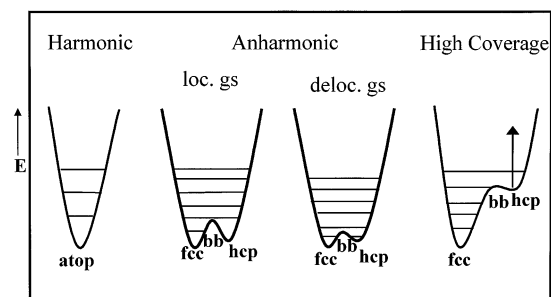

Figure 11. Schematic potential curves for hydrogen bonded in a harmonic potential (such as atop), anharmonic potentials (localized and delocalized ground state), and hydrogen bonded at high coverage, showing the effect of H−H lateral interactions at high coverage. The exact extent of the delocalization in the ground vibrational state has been somewhat controversial.

or no fcc−hcp sites exist on flat surfaces, i.e., all sites appear near edges or corners.

The presence of the 550-cm^{-1} peak in the gas-phase IR data[73] suggests the presence of delocalized H, but this peak may only reflect the nature of the vibrationally excited H existing after the vibrational excitation. Almost all recent theoretical calculations of the final vibrationally excited state at 550 cm^{-1} (68 MeV) find that this state is delocalized over the fcc/bridged/hcp sites.[68] However, the nature of the H in the ground state at low coverages on Pt is still unclear even in the gas phase, and certainly it is unclear in the electrolyte. The recent calculations of Badescu et al.[11] and those of Kallen and Wahnstrom[12] indicate that the ground state is localized in the fcc sites but that it contains a significantly large lateral vibrational amplitude. The recent LDF calculations of Nobuhara et al.[13,14] on the other hand indicate that the ground state for Pt is already spread out over the fcc/hcp sites. Quite interesting, all three calculations accurately predict a weak feature around 24 eV, seen in some EELS spectra and the 68-meV feature. In this work, the interpretation of the new XANES data and previously published EMIRS data provide some evidence that at low coverage the H is already delocalized in the ground state.

The nature of the delocalized H, and the reason it delocalizes on the Pt (111), can be understood from the schematic potentials in Figure 11. Figure 11 shows a typical harmonic oscillator potential with vibrational levels given by $E_v = (v + {}^1/_2)h\nu$ and ν given by $(1/(2\pi))(k/m_H)^{1/2}$, with k the force constant and the Pt−H reduced mass effectively equal to the H mass, m_H. Because m_H is rather small, the zero-point energy, ${}^1/_2h\nu$, is large. The zero-point energy can be reduced by reducing the effective force constant k, and since the difference in energy for the 3 sites, fcc, bridged, and hcp, is rather small as illustrated in Figure 11, the H atom prefers to be delocalized at low coverage over the fcc/bridged/hcp sites. With increasing coverage, the energy of the hcp site increases, as illustrated, because of lateral interactions making the H atom eventually localize into the fcc site. The small vibrational spacing is confirmed by the experimentally observed 500 cm^{-1} peak, but the exact extent of the delocalization in the ground state, $v = 0$, is still very controversial.

B. Comparison of Pt L$_{23}$ XAS Data from Electrochemical Cell with Gas-Phase Data and Theory. Figure 12 compares Pt L$_3$ $\Delta\mu$ data from this work with that recently reported by Oudenhuijzen et al.[83] for H adsorption on Pt clusters ($N = 6.5$) supported on Al$_2$O$_3$ in the gas phase. Their samples were reduced in H at 672 K and then heated in a vacuum at 322 K. The $\Delta\mu$ spectra were then obtained by taking the difference $\mu(H_{red}) - \mu(322)$. According to the TPD data mentioned above, these difference spectra should represent the localized fcc H

H Adsorption Sites on Pt/C Electrodes
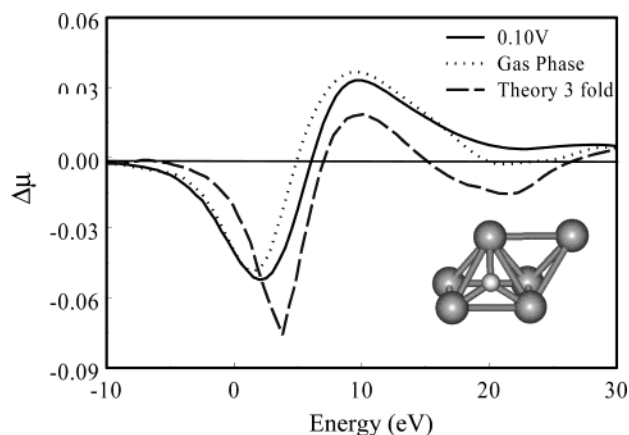
J. Phys. Chem. B, Vol. 108, No. 7, 2004 **2339**

Figure 12. Comparison of $\Delta\mu$ difference spectra for H in the 3-fold sites: experimental gas-phase data (solid line), $\Delta\mu(H_{red}) - \mu(vac\ 322\ K)$,[83] experimental at 0.1 V RHE from Figure 3 (dotted line), and FEFF8 calculations from Figure 6. Data were aligned and normalized for optimal agreement.
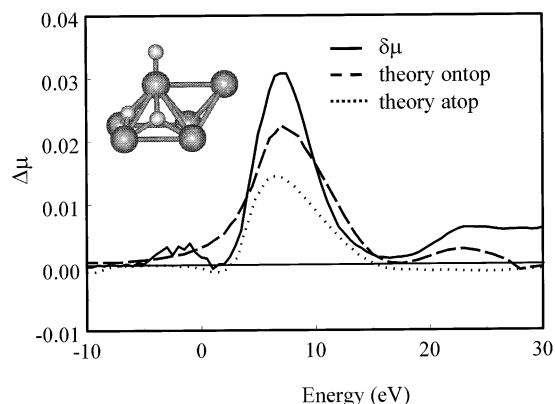

Figure 13. Comparison of experimental $\delta\mu(0.0\ V) = \Delta\mu(0.0\ V) - 2.5\Delta\mu(0.1\ V)$ with the theoretical atop signature from Figure 6 ($\Delta\mu$(atop)) and with FEFF8 calculations taking the difference $\delta\mu$(ontop) $= \mu(H_{atop}+H_{fcc}/Pt_6) - \mu(H_{fcc}/Pt_6)$ as described in the text. The qualitative agreement in spectral shape strongly suggests the existence of atop H on top of the 3-fold H near 0.0 V as illustrated.

on the flat faces. These data are compared with our difference spectra $\Delta\mu(0.1\ V) = \mu(0.1\ V) - \mu(0.54\ V)$ and with our theoretical $\Delta\mu = \mu(H/Pt_6) - \mu(Pt_6)$ results for fcc H in Figure 12. The different $\Delta\mu$ were aligned and normalized for optimal agreement. The agreement in spectral shape between these $\Delta\mu$, although not quantitiative, is sufficient to indicate that at 0.1 V the spectra are reflecting localized fcc H at intermediate coverages on the flat faces.

Although $\Delta\mu(0.0\ V)$ appears to have a spectral line shape qualitatively similar to that of $\Delta\mu(0.1\ V)$, Figure 13 shows that the weighted difference

$$\delta\mu(x) = \Delta\mu(0.0\ V) - x\Delta\mu(0.1\ V) \qquad (2)$$

has a very different spectral shape than either $\Delta\mu$. The variable $x = 2.5$ in Figure 13 was chosen so as to minimize the average intensity in $\delta\mu$ over as large an energy range as possible. On the basis of previous Raman data,[77,78] one can assume that $\Delta\mu(0.0\ V) = a[3f] + b[atop]$ and $\Delta\mu(0.1\ V) = a'[3f] + b'[atop]$, where $b < a$, $b' < a'$, and $b' < b$. Then a weighted difference gives $\delta\mu(x) = (b - xb')[atop]$, where x is chosen so that $a - xa' = 0$. The different spectral shape of $\delta\mu$ shows that a small but quantitative difference does indeed exist between the two $\Delta\mu$ line shapes.
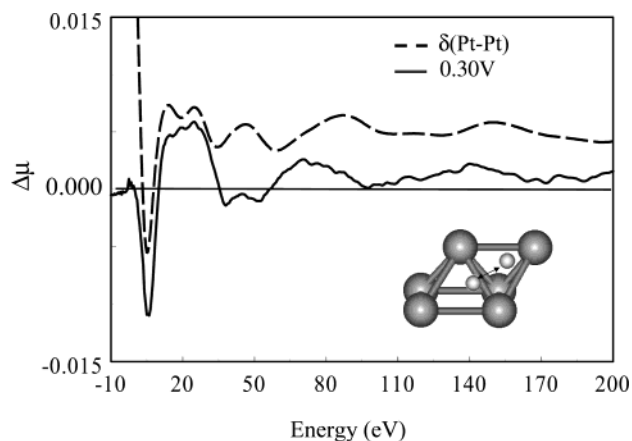
Figure 14. Comparison of the experimental $\Delta\mu(0.3\ V)$ spectrum from Figure 3 with Pt−Pt EXAFS features obtained by taking the difference $\delta(Pt-Pt) = 0.1[1 - \mu_{L3}(0.54\ V)]$.

A comparison of $\delta\mu(0.0\ V)$ with the theoretical result

$$\delta\mu(ontop) = \mu(H_{atop}H_{fcc}/Pt_6) - \mu(H_{fcc}/Pt_6) \qquad (3)$$

calculated with FEFF8 is also shown in Figure 13. Here $H_{atop}H_{fcc}/Pt_6$ represents a cluster with 1 atop and 2 fcc Hs on the Pt_6 cluster as shown in the inset of Figure 13, while H_{fcc}/Pt_6 represents the normal 2 fcc H on the Pt_6 clusters as shown in Figure 6. The reasonable agreement between theory and experiment confirms the presence of atop H in addition to the fcc H at 0.0 V (we shall call this ontop H). The presence of ontop H has been indicated previously by several Raman and SNIFTER investigations,[77,78] which show the growth of the 2000-cm^{-1} peak with decreasing potential below 0.2 V.

The spectral line shape for the theoretical $\delta\mu$(ontop) in Figure 13 is somewhat similar to the FEFF8 results for $\Delta\mu$(atop) also given in Figure 13. This suggests that the presence of the fcc H present at these same sites does not dramatically change the signature for the atop H but does alter it. The change arises in part because the ontop H has a longer Pt−H bond length than the much stronger bonded atop, and hence, the Pt−H bond length is longer for the ontop H. Therefore, the ontop H gives a $\Delta\mu$ signature with a longer wavelength compared to the fcc H, a difference most notable above 20 eV. FEFF8 results with changing Pt−H bond length confirm this wavelength change (the atop calculated with Pt−H distance of 1.8 Å and the ontop 2.0 Å); indeed, the Pt−H bond length can be approximately determined as in Figure 13 by optimizing agreement between the FEFF8 results and the experimental data.

The experimental $\Delta\mu(0.3\ V)$ has a significantly different character than that at 0.0 and 0.2 V, particularly at larger energies. Indeed, at higher energies the structure is very similar to the normal Pt−Pt EXAFS features. To show this, Figure 14 compares the $\Delta\mu(0.3\ V)$ line shape over an extended energy range with the spectrum $\delta\mu(Pt-Pt) = a(1 - \mu_{L3}(0.54))$, where a is an arbitrary normalization constant. Here $\delta\mu(Pt-Pt)$ basically emphasizes the Pt−Pt EXAFS features. The similarity between the two line shapes is quite good, except for a small energy shift above 55 eV. This suggests strongly that Pt−Pt EXAFS features are visible in the $\Delta\mu(0.3\ V)$ arising from a reduction in Pt−Pt scattering at 0.3 V, but no direct Pt−H scattering is visible in $\Delta\mu(0.3\ V)$. At this potential, the H coverage is low and thus the H could be delocalized over the fcc/bridge/hcp sites as discussed above, making the H invisible in the XANES spectrum.

What is the cause for the reduction in Pt−Pt EXAFS scattering in the 0.3 V data compared to 0.54 V? Three
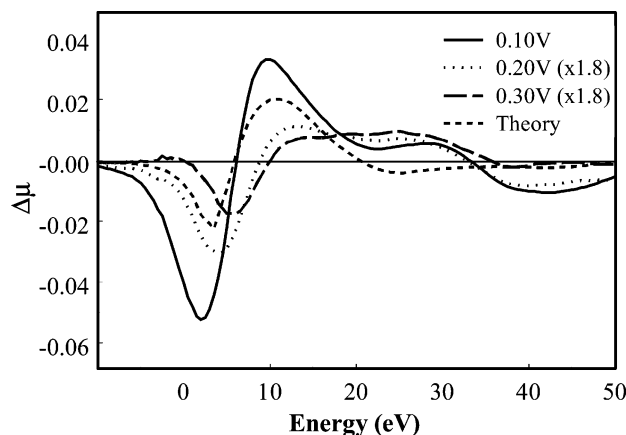
Figure 15. Comparison of the experimental $\Delta\mu$(0.3 V) data with scaled data at other potentials, 1.8 $\Delta\mu$(0.2) and 1.8 $\Delta\mu$(0.1), and with FEFF8 results assuming a Pt−H distance of 1.8 Å. The excellent agreement between the three experimental $\Delta\mu$ values in the region of 15−25 eV suggests strongly that the signal here arises from δ(Pt−Pt) scattering. Therefore, the H scattering contributes only below this region, and the shift below 5 eV between the 0.2 and 0.3 spectra probably arises from the relative weighting of Pt−H vs δ(Pt−Pt) scattering.

possibilities can be given. Either (a) the Pt−Pt distance is increased by the presence of the H, (b) the Pt−Pt coordination number is decreased due to a cluster morphology change, or (c) the Pt−Pt scattering is reduced at low k because of a Pt−Pt bond strength weakening. Arguments are given below for favoring mechanism c, and rejecting mechanisms a and b.

(a) Pt−Pt Elongation. The presence of H is known to relax the contraction in the Pt−Pt distance, which occurs near the surface on clean Pt, and is confirmed by the EXAFS results in Table 1. Typically the Pt−Pt distance of 2.77 Å in bulk Pt contracts to around 2.70 Å in small Pt particles.[84] This decrease is much less in Table 1, because of the rather large cluster size; the EXAFS gives the average Pt−Pt distance, and only the near-surface Pt−Pt distance is changing. Since clusters around 2 μm have a dispersion around 50% (i.e., only half of the Pt atoms are surface atoms), the 2.74 Å value in Table 1 is qualitatively consistent with this expectation, i.e., 2.74 $\approx$ (2.77$_{bulk}$ + 2.70$_{surface}$)/2. The adsorption of H relaxes this contraction, increasing the average Pt−Pt distance, and could decrease the EXAFS intensity relative to the clean cluster. The increase in Pt−Pt distance has actually been used to follow the adsorption of H on a particle surface.[85]

The small Pt−Pt XANES features (due to reduction of Pt scattering relative to 0.54 V) are present in all of the $\Delta\mu$ spectra of Figure 5, indeed it is increasing with H coverage, as shown in Figure 15 particularly around 20−30 eV, but the large Pt−H scattering between −5 and 20 eV for the data taken at 0.1 V masks the δ(Pt−Pt) scattering below 20 eV. At 0.3 V, the Pt−H scattering is nearly invisible, so the δ(Pt−Pt) scattering is clearly observed throughout the energy range. The data for 0.2 V clearly has contributions from both direct Pt−H scattering and the δ-(Pt−Pt) scattering.

We conclude that the reduction in Pt−Pt EXAFS scattering with adsorption of H could arise from an increase in the Pt−Pt distance; however, the EXAFS results in Table 1 do not show this relaxation and elongation of the Pt−Pt distance until very large H coverages (lower potentials).

(b) Cluster Morphology Change. We reject mechanism a and consider mechanism b, a change in the shape of the cluster as another possibility at 0.3 V. A reduction in N could arise from a flattening of the Pt cluster as H is deposited on the surface. However, this is in contradiction to that usually found in the
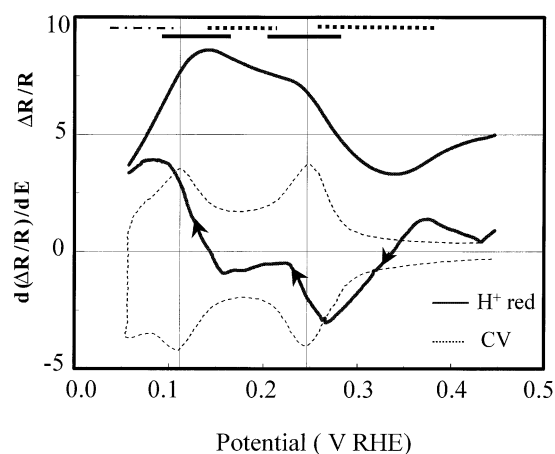

Figure 16. Comparison of previously reported EMIRS data,[26] along with the CV curve. The original EMIRS (d($\Delta R/R$)dE) is shown along with our integrated data $SR = \Delta R/R = \int [b + (d(\Delta R/R)/dE)]\ dE + C$, where C is chosen to make $SR = 0.0$ at 0.5 V and b is chosen to minimize the SR amplitude. The lines near the top show the regions where delocalized H (dashed line), 3-fold H (solid line), and atop H (dotted line) are adsorbing on the surface.

gas phase[84] when H adsorption makes the Pt particle more round as indicated by a small increase in N, as seen in Table 1 at high coverage (assuming such a small increase is statistically significant).

(c) Pt−Pt Bond Strength Change. By the rejection of mechanisms a and b, we attribute the decrease in Pt−Pt scattering due to c, a decrease in Pt−Pt bond strength. This is entirely consistent with the FEFF8 results in Figure 6, which show a decrease in Pt−Pt scattering due to a weakening of the Pt−Pt bonding upon adsorption of H as discussed above. This bond weakening causes a reduction in Pt−Pt scattering only at relatively low energies, where the electronic and multiple scattering effects dominate, as seen clearly in the $\Delta\mu$ below 100 eV, but not in the EXAFS because of the much longer k range utilized in the EXAFS. Apparently the bond weakening is occurring already with initial adsorption of delocalized H, as seen in the XANES, but the elongation of the Pt−Pt bond does not occur, or at least is not visible in the EXAFS, until higher coverages of localized H.

The significant δ(Pt−Pt) scattering at 0.3 V suggests that something significant has happened at the cluster surface, yet the Pt−H scattering is not seen directly in the experimental $\Delta\mu$ data. If the H were delocalized on the surface, the very large Debye−Waller factor, $\Delta\sigma^2$, reflecting the large lateral oscillations on the surface, would indeed sharply diminish the Pt−H scattering

$$\chi(k) = F(k) \exp(-2k^2\sigma^2) \sin(2kR + \varphi) \qquad (4)$$

In eq 4, all irrelevant factors are included in $F(k)$ to emphasize the diminishing effect that the Debye−Waller factor has on the normal scattering intensity. It appears that the $\Delta\mu$ signature for delocalized H in eq 1 is just the $\Delta[\mu_o\chi_{Pt-Pt}]$ term with the $\mu_{o,H}\chi_{Pt-H}$ term essentially zero. These results indicate that, at a minimum, the H must have a large lateral vibrational amplitude at 0.3 V, but the almost complete lack of Pt−H scattering in $\Delta\mu$(0.3 V) all the way down to the edge suggests that the H may be totally delocalized over the fcc/bridged/hcp sites even in the ground vibrational state in the electrochemical cell.

C. Further Evidence for Delocalized H from EMIRS Data. Strong supporting evidence for the delocalization of the H at low coverage on Pt even in the electrolyte is available from

H Adsorption Sites on Pt/C Electrodes

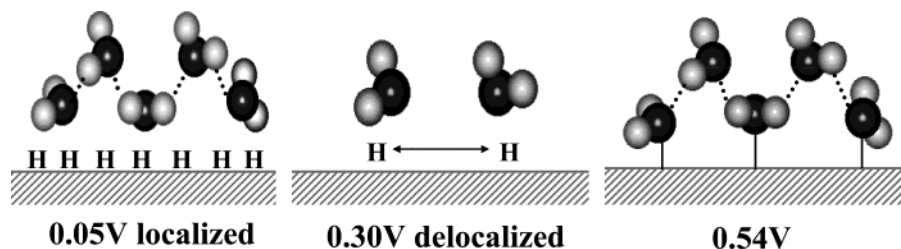*J. Phys. Chem. B, Vol. 108, No. 7, 2004* **2341**

Figure 17. Schematic showing the water double layer on clean Pt and on the localized H, with disruption of the double layer in the presence of delocalized H.

previously published Pt surface reflectivity data of Nichols and Bewick.[45] Here the changes in the reflectivity of a highly polished polycrystalline Pt electrode surface is measured in 0.1 M H_2SO_4 at IR frequencies. In their work, $\Delta R/R$ is obtained by modulating the applied potential between 0.05 V RHE and some other voltage V and obtaining the difference $\Delta R/R = [R(V) - R(0.05)]/R(0.05)$. In a plot of $\Delta R/R$ with wavelength (not shown), a relatively strong absorption peak appears around 1.9 μm. This peak has been attributed to the combination absorption band $\nu_2 + \nu_3$ (asymmetric + bending modes) of water. By changing V with wavelength fixed at 1.9 μm, a plot of $d(\Delta R/R)/dV$ vs voltage can be obtained as shown in Figure 16 along with the CV data. Nichols and Bewick interpreted these changes in reflectivity as resulting from changes in the orientation of water in the double layer and hence to changes in the degree or nature of water H bonded to the Pt surface or H-covered surface. Although these data were published over 20 years ago, full understanding of these changes in H bonding has never been given. We believe these data give strong evidence for the existence of delocalized H at low coverages.

Figure 16 reveals a strong variation in the Pt reflectivity, $d(\Delta R/R)/dE$ in the H-absorption region with reproducible minima around 0.28 and 0.15 V RHE. These potentials mark the minimum point (maximum H coverage) where delocalized H can still exist on the edge and flat surfaces respectively, as indicated by the dotted lines near the top of Figure 16. Below these potentials, the H begins localization into the fcc sites as the coverage increases to its maximum value on these respective sites at 0.25 and 0.12 V as indicated by the vertical lines. Figure 16 also shows integrated reflectivity data $SR = \int [b + (d(\Delta R/R)/dE)]dV + C$, where C is chosen to make $SR = 0.0$ at 0.5 V and b is chosen to minimize the SR amplitude. In Figure 16, $SR = \Delta R/R$ clearly shows a minimum around 0.33 V where the presence of delocalized H should be large, and maxima right at the peaks in the CV curves where the H is expected to reach near-maximum coverage in the fcc sites at the respective face and corner sites.

The existence of H bonding between the water molecules and the Pt surface is well known in the double layer. The absorption of H and its hopping from site to site is expected to disrupt this double layer or water network on the surface as illustrated in Figure 17. Even if the H hopping is slow, it probably is faster than the time needed to re-establish the H-bonded water network above it. Thus the partially delocalized H on the surface decreases the reflectivity. As the H localizes with coverage, the double layer is re-established above the H monolayer, and the reflectivity is restored to essentially that which it was on the clean surface. The decrease of the SR intensity below 0.12 V RHE, as the atop H is deposited on the surface "on top" of the 3-fold H, is interesting. It may reflect a diminishing of the double-layer water and the beginning of conditions for the H evolution reaction. It has been observed previously with EMIRS[86] and is consistent with the EXAFS
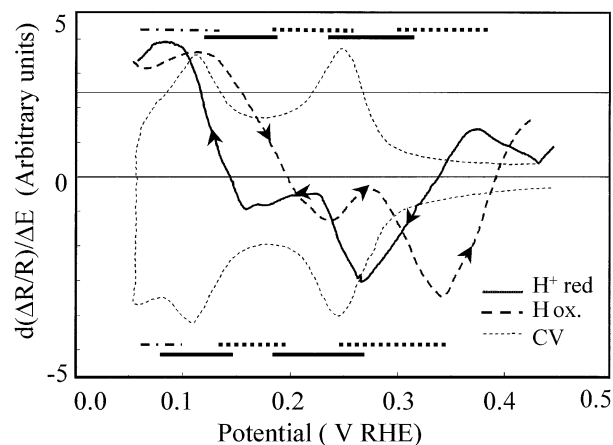

Figure 18. Comparison of previously reported EMIRS data[26] for reduction and oxidation showing a large "hysteresis" effect. The lines near the top and bottom show the regions where delocalized H (dashed line), 3-fold H (solid line), and atop H (dash-dotted line) are adsorbing or desorbing from the surface.
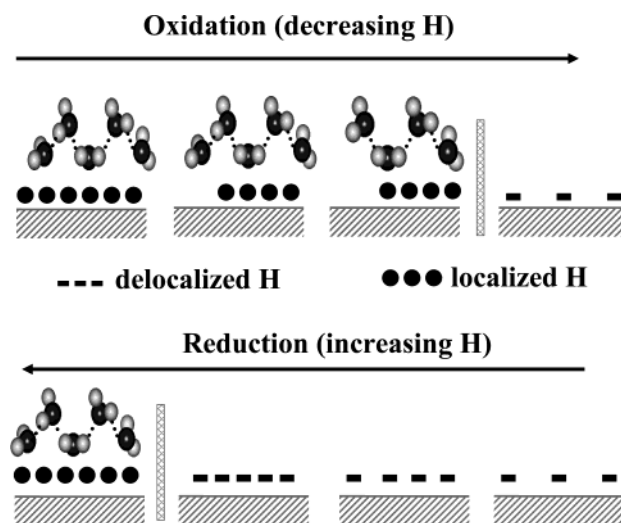

Figure 19. Schematic showing the localized H (large filled dots) and delocalized H (short dashes) with increasing/decreasing H on the surface, illustrating the mechanism for the hysteresis in the localization of H, which drives the hysteresis in the formation of the water double layer as described in the text.

coordination discussed above. Much further work is required here to totally understand this reduction in SR below 0.1 V.

Figure 18 compares the reflectivity data of Nichols and Bewick[45] under reduction and oxidation. The reflectivity data clearly show a large hysteresis effect, while nearly none is visible in the CV curve. Figure 19 schematically shows why this may be happening. The delocalized and localized H are indicated by the short lines and filled circles, respectively. The total H coverage increases upon going to the left (lower potential). In reduction, the water double layer does not form
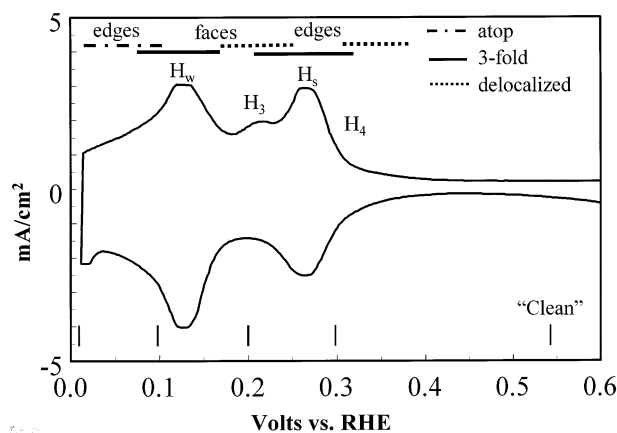
Figure 20. CV data[86] illustrating the "third anodic" peak (H_3) along with the regions for strong and weakly bonded H (H_s and H_w) and the fourth anodic region (H_4). Also shown are the results from this paper for atop, delocalized, and 3-fold H.

until the H localizes into the fcc sites, which does not occur until significant H coverage exists as illustrated. Upon initial oxidation, the water double layer is already formed, and the H does not delocalize until significant H is removed, i.e., there is a hysteresis in the critical H coverage where the localization/delocalization phenomenon occurs, and localization allows the formation of the double layer. The hysteresis occurs because, as long as the H is delocalized, the H can move about the surface to minimize the lateral interactions and thereby delay the localization with increasing coverage as long as possible. This occurs with reduction. Starting with localized H, the H is much less mobile, and assuming the H leaves from the localized island edge sites, the lateral interaction effects stay large, and therefore the H remains localized to lower coverages in H.

D. Delocalized H and the "Third Anodic" Peak. Figures 16 and 18 suggest regions where the delocalized H should be active. The presence of delocalized H provides a possible straightforward explanation for the well known but controversial "third anodic" peak present in the anodic current around 0.22 V in many CV curves (see Figure 20).[87] It has been called the third anodic peak (H_3) to distinguish it from the other two larger peaks, namely, the feature around 0.12 V RHE arising from H on (111) like faces (or weakly bound H, H_w) and that around 0.28 V due to H on the edges (or strongly bound H, H_s). It is called an anodic peak because it is only seen in the anodic (oxidation of H) curve. A comparable fourth anodic peak (H_4) around 0.34 V has also been mentioned by Frelink et al.[87] and is barely visible in Conway's CV curve in Figure 20.[86]

The source of H_3 has been assigned to a plethora of different species by many different authors. These have been summarized by Frelink et al.[87] as (a) absorbed H (i.e., H below the surface), (b) absorbed or underpotentially deposited H_2 below the surface, (c) H_3^+ species on the surface, (d) H in specific defect sites, and even (e) Pt−OH species (see references in Frelink et al.).[87] Its character has been extensively studied, and this character may be consistent with attributing H_3 and H_4 to the onset of delocalized H with decreasing coverage, on the faces and at edges, respectively. Note that the EMIRS data for the anodic scan in Figure 18 is not only shifted to higher potential but its shape suggests a stronger transition between the local and delocalized H, and this transition fall rights near the H_3 peak potential.

The characteristics of the H_3 peak as reported previously by other authors are as follows:[86,87]

(a) It is connected to the H_W peak, i.e., as the H_W intensity decreases, the H_3 peak increases.

(b) The potential must be brought below 0.08 V in the cathodic scan in order for H_3 to appear in the anodic scan and grows with the time up to 100 s when the potential held below 0.07 V is cathodic.

(c) It appears only at slow scan rates and shows irreversible behavior even at very low scan rates.

(d) Taking the electrode above 1.1 V and then recycling as well as adsorption of Cl^- and Br^- increases H_3.

Point a is totally consistent with an H_3 assignment to the involvement of delocalized H on the faces, and point b is suggestive of Figure 19, which shows that localization must occur at lower potential in the cathodic scan before the local/delocal transition can occur in the anodic scan. The strong hysteresis in Figure 19 and the connection of the double layer with the delocalized H is suggestive of points b and c, concerning irreversible behavior and response time. The presence of adsorbates (O due to scanning above 1.1 V) may increase lattice interactions on the surface, which possibly enhances the localization of the H, thereby making the local/delocal transition more visible.

The straightforward explanation for these anodic peaks to the onset of delocalized H because of their position relative to H_w and H_s in the CV curve provides further evidence for the very existence of delocalized H in aqueous environments. However, much more work must be performed to definitely show that the local-delocalized H transition, and the role of the double layer in this transition, is consistent with the observed character of the H_3 peak. Such work could fully confirm that delocalized H is involved with the production of these anodic peaks and hence fully confirm the existence of delocalized H.

Summary

Pt $L_{2,3}$ XANES data taken in situ on a Pt electrode surface in an electrochemical cell, along with detailed analysis and FEFF8 calculations, has provided in exceptional detail the nature of H adsorbed on a Pt electrode, in contrast to the normal EXAFS data and analysis, which shows almost no effects due to H adsorption. Comparison of results with previous results for H adsorption in the gas phase shows that the H adsorption sites change with coverage in essentially the same way in the two cases. These results confirm that the 0.25-V peak arises from H adsorption on defects and edges and the 0.1-V peak from H adsorption on the flat faces. Further in the range of 0.1−0.0 V, more H weakly adsorbs in the atop geometry on the edge sites "ontop" of nearby fcc H confirming previous vibrational spectroscopy results. Finally, a comparison of XANES data with FEFF8 calculations, along with previously published Pt reflectivity data, provides strong evidence that at low coverages on Pt, in an electrolyte and probably also in the gas phase, H is highly mobile and probably undergoes relatively fast hopping between fcc and hcp sites even in the ground vibrational state. The presence of delocalized H and its onset in an anodic scan provides a possible straightforward explanation for the position and curious behavior of the third and fourth anodic CV peaks, but further work is required to confirm this point.

H Adsorption Sites on Pt/C Electrodes

J. Phys. Chem. B, Vol. 108, No. 7, 2004 **2343**

References and Notes

(1) Peremans, A.; Tadjeddine, A. *J. Chem. Phys.* **1995**, *103* (6), 7197−7203.

(2) Lu, K. E.; Rye, R. R. *Surf. Sci.* **1974**, *45*, 677−695.

(3) Ogasawara, H.; Ito, M. *Chem. Phys. Lett.* **1994**, *221*, 213−218.

(4) Tidswell, I. M.; Markovic, N. M.; Ross, O. N. *J. Electroanal. Chem.* **1994**, *376* (1−2), 119−126.

(5) Christmann, K.; Ertl, G. *Surf. Sci.* **1976**, *60* (12), 365−384.

(6) Lui, K. M.; Kim, Y.; Lau, W. M.; Rabalais, J. W. *Appl. Phys. Lett.* **1999**, *75* (4), 587−589.

(7) Takagi, N.; Yasui, Y.; Takaoka, T.; Sawada, M.; Yanagita, H.; Aruga, T.; Nishijima, M. *Phys. Rev. B.* **1996**, *53* (20), 13767−13771.

(8) Puska, M. J.; Nieminen, R. M.; *Surf. Sci.* **1985**, *157*, 413−435.

(9) Tsuchiya, S.; Amenomiya, Y.; Cvetanovic, R. J. *J. Catal.* **1971**, *19* (3), 245−255.

(10) Al-Akl, A.; Attard, G.; Price, R.; Timothy, B. *Phys. Chem. Chem. Phys.* **2001**, *3* (16), 3261−3268.

(11) Badescu, S. C.; Salo, P.; Ying, S. C.; Jacobi, K.; Wang, Y.; Berdurftig, K.; Ertl, G. *Phys. Rev. Lett.* **2001**, *88* (13), 136101−136104.

(12) Kallen, G.; Wahnstrom, G. *Phys. Rev. B.* **2001**, *65* (3), 334061−334063.

(13) Nobuhara, K.; Nakanishi, H.; Kasai, H.; Okiji, A. *J. Appl. Phys.* **2000**, *88* (11), 6897−6901.

(14) Nobuhara, K.; Nakanishi, H.; Kasai, H.; Okiji, A.; *J. Appl. Phys.* **2002**, *91* (4), 1855−1859.

(15) Christmann, K. *Surf. Sci. Rep.* **1988**, *9* (1−3), 1−163.

(16) Marković, N. M.; Ross, P. N., Jr. *Surf. Sci. Rep.* **2002**, *45* (4−6), 117−229.

(17) Xu, X.; Wu, D. Y.; Ren, B.; Xian, H.; Tian, Z. Q. *Chem. Phys. Lett.* **1999**, *311* (3−4), 193−201 and references therein.

(18) Prinz, H.; Strehblow, H. H. *Electrochem. Acta* **2002**, *47* (19), 3093−3104.

(19) Wang, H.; Tobin, R. G.; Lambert, D. K.; Fisher, G. B.; DiMaggio, C. L. *Surf. Sci.* **1995**, *330* (2), 173−181.

(20) Teliska, M.; O'Grady, W. E.; Ramaker, D. E. In preparation.

(21) Greenlief, C. M.; Akhter, S.; White, J. M. *J. Phys. Chem.* **1986**, *90* (17), 4080−4083.

(22) Zolfaghari, A.; Chayer, M.; Jerkiewicz, G. *J. Electrochem. Soc.* **1997**, *144* (9), 3034−3040.

(23) Gao, L.; Conway, B. E. *Electrochim. Acta* **1994**, *39* (11−12), 1681−1693.

(24) Kua, J.; Goddard, W. A. *J. Phys Chem. B.* **1998**, *102* (47), 9481−9491.

(25) Bewick, A.; Russell, J. W. *J. Electroanal. Chem. Inter. Electrochem.* **1982**, *132*, 329−344.

(26) Bewick, A.; Kunimatsu, K.; Robinson, J.; Russell, J. W. *J. Electroanal. Chem. Inter. Electrochem.* **1981**, *119* (1), 175−185.

(27) Eisert, F.; Elg, A. P.; Rosen, A. *Appl. Phys. A: Mater. Sci. Process.* **1995**, *A60* (2), 209−215.

(28) Lipkowski, J.; Stolberg, L.; Yang, D. F.; Pettinger, B.; Mirwald, S.; Henglein, F.; Kolb, D. M. *Electrochim. Acta* **1994**, *39* (8−9), 1045−56.

(29) Rodes, A.; Zamakhchari, M. A.; Achi, K.; Clavilier, J. *J. Electroanal. Chem. Inter. Electrochem.* **1991**, *305* (1), 115−129.

(30) Markovic, N. M.; Grugur, B. N.; Ross, P. N. *J. Phys. Chem. B* **1997**, *101* (27), 5405−5413.

(31) Lamy-Pitara, E.; El Mouaid, S.; Barbier, *J. Electrochim. Acta* **2000**, *75* (1−4), 4299−4308.

(32) Kolics, A.; Wieckowski, A. *J. Phys. Chem. B* **2001**, *105* (13), 2588−2595.

(33) Zolfaghari, A.; Jerkiewicz, G. *J. Electroanal. Chem.* **1997**, *420* (1−2), 11−15.

(34) Koningsberger, D. C.; Prins, R. In *X-ray Absorption Spectroscopy*; John Wiley & Sons: New York, 1988.

(35) Ramaker, D. E.; Mojet, B. L.; Koningsberger, D. C.; O'Grady, W. E. *J. Phys.: Condens. Matter* **1998**, *10* (39), 8753−8770.

(36) O'Grady, W. E.; Ramaker, D. E. *Electrochim. Acta* **1998**, *44* (8−9), 1283−1287.

(37) van Dorssen, G. E.; Koningsberger, D. C.; Ramaker, D. E. *J. Phys.: Condens. Matter* **2002**, *14* (49), 13529.

(38) Ramaker, D. E.; Mojet, B. L.; Miller, J. T.; Koningsberger, D. C. *Top. Catal.* **2000**, *10* (3−4), 157−165.

(39) Koningsberger, D. C.; Mojet, B. L.; Miller, J. T.; Ramaker, D. E. *J. Synchrotron Radiat.* **1999**, *6* (3), 135−145.

(40) Ramaker, D. E.; O'Grady, W. E. *J. Synchrotron Radiat.* **1999**, *6* (3), 800−802.

(41) O'Grady, W. E.; Qian, X.; Ramaker, D. E. *J. Phys. Chem. B* **1997**, *101* (29), 5624−5626.

(42) Ramaker, D. E.; Qian, X.; O'Grady, W. E. *Chem. Phys. Lett.* **1999**, *299* (2), 221−224.

(43) Ramaker, D. E.; Koningsberger, D. C. *Phys. Rev. Lett.* **2002**, *89* (13), 139701.

(44) Ankudinov, A. L.; Rehr, J. J.; Low, J.; Bare, S. R. *Phys. Rev. Lett.* **2001**, *86* (8), 1642−1645.

(45) Nichols, R. J.; Bewick, A. *J. Electroanal. Chem.* **1988**, *243* (2), 445−453.

(46) Soldatov, A. V.; Della Longa, S.; Bianconi, A. *Solid State Commun.* **1993**, *85*, 863−868.

(47) Reifsnyder, S. N.; Otten, M. M.; Sayers, D. E.; Lamb, H. H. *J. Phys. Chem. B.* **1997**, *101* (25), 4972−4977.

(48) Mukerjee, S.; McBreen, J. *J. Electrochem. Soc.* **1996**, *143* (7), 2285−2294.

(49) Lytle, F. W.; Greegor, R. B.; Marques, E. C.; Biebesheimer, V. A.; Sandstrom, D. R.; Horsley, J. A.; Via, G. H.; Sinfelt, J. H. *ACS Symp. Ser.* **1985**, *288*, 280−293.

(50) Samant, M. G.; Boudart, M. *J. Phys. Chem.* **1991**, *95* (10), 4070−4074.

(51) Asakura, K.; Kubota, T.; Ichikuni, N.; Iwasawa, Y. *Stud. Surf. Sci. Catal.* **1996**, *101* (B), 911−919.

(52) Boyanov, B. I.; Morrison, T. I. *J. Phys. Chem.* **1996**, *100* (40), 16318−16326.

(53) Mansour, A. N.; Cook, J. W., Jr.; Sayers, D. E. *J. Phys. Chem.* **1984**, *88* (11), 2330−2334.

(54) J. McBreen, J.; O'Grady, W. E.; Pandya, K. I.; Hoffman, R. W.; Sayers, D. E. *Langmuir* **1987**, *3* (3), 428−433.

(55) WinXAS 97 copyright Thorsten Ressler 1992−1997, http://our-world.compuserve.com/homepages/t_ressler, Ressler, T. *J. Physique IV* **1997**, *7*, C2−269.

(56) Koningsberger, D. C.; de Graaf, J.; Mojet, B. L.; Ramaker, D. E.; Miller, J. T. *Appl. Catal.* **2000**, *191* (1−2), 205−220.

(57) Mojet, B. L.; Miller, J. T.; Ramaker, D. E.; Koningsberger, D. C. *J. Catal.* **1999**, *186* (2), 373−386.

(58) Ramaker, D. E.; Mojet, B. L.; Garriga Oostenbrink, M. T.; Miller, J. T.; Koningsberger, D. C. *Phys. Chem. Chem. Phys.* **1999**, *1* (9), 2293−2302.

(59) Koningsberger, D. C.; Oudenhuijzen, M. K.; Bitter, J. H.; Ramaker, D. E. *Top. Catal.* **2000**, *10* (3−4), 167−177.

(60) Mojet, B. L.; Ramaker, D. E.; Miller, J. T.; Koningsberger, D. C. *Catal. Lett.* **1999**, *62* (1), 15−20.

(61) Zabinsky, S. I.; Rehr, J. J.; Aukudinov, A.; Albers, R. C.; Eller, M. J. *Phys. Rev. B: Condens. Matter* **1995**, *52* (4), 2995−3009.

(62) Ankudinov, A. L.; Ravel, B.; Rehr, J. J.; Bare, S. *Phys. Rev. B* **1998**, *58* (12), 7565−7576.

(63) Ankudinov, A. L.; Rehr, J. J.; Low, J. J.; Bare, Simon R. *J. Chem. Phys.* **2002**, *116* (5), 1911−1919.

(64) Janin, E.; von Schenck, H.; Gothelid, M.; Karlsson, U. O. *Phys Rev. B* **2000**, *61* (19), 144−149.

(65) de Graaf, J.; van Dillen, A. J.; de Jong, K. P.; Koningsberger, D. C. *J. Catal.* **2001**, *203*, 307−321. (b) de Graaf, J. Ph.D. Dissertation, Utrecht University, Ridderkerk, 2001.

(66) Koningsberger, D. C.; Oudenhuijzen, M. K.; de Graaf, J.; van Bokhoven, J. A.; Ramaker, D. E. *J. Catal.* **2003**, *216* (1−2), 178−191.

(67) Feibelman, P. J. *Phys. Rev. B: Condens. Matter* **1997**, *56* (16), 10532−10537.

(68) Papoian, G.; Norskov, J. K.; Hoffman, R. *J. Am. Chem. Soc.* **2000**, *122* (17), 4129−4144.

(69) Ko, C. S.; Gorte, R. J. *Surf. Sci.* **1985**, *161* (2−3), 597−607.

(70) Lui, K. M.; Kim, Y.; Lau, W. M.; Rabalais, J. W. *J. Appl. Phys.* **1999**, *86* (9), 5256−5262.

(71) Davis, S. M.; Somorjai, G. A. *Surf. Sci.* **1985**, *161* (2−3), 597−607.

(72) Thomas, V. D.; Schwank, J. W.; Gland, J. L. *Surf. Sci.* **2002**, *501* (3), 214−234.

(73) Baro, A. M.; Ibach, H.; Bruchmann, H. D. *Surf. Sci.* **1979**, *88* (2−3), 384−389.

(74) Nakamura, M.; Song, M. B.; Ito, M. *Chem. Phys. Lett.* **2000**, *320* (5−6), 381−386.

(75) Tadjeddine, A.; Peremans, A.; Guyot-Sionnest, P. *Surf. Sci.* **1995**, *335* (1−3), 210−220.

(76) Zheng, W. Q.; Pluchery, O.; Tadjeddine, A. *Surf. Sci.* **2002**, *490−497*, 502−503.

(77) Xu, X.; Ren, B.; Wu, D. Y.; Xian, H.; Lu, X.; Shi, P.; Tian, Z. Q. *Surf. Interface Anal.* **1999**, *28* (1), 111−114.

(78) Ren, B.; Huang, Q. J.; Cai, W. B.; Mao, B. W.; Liu, F. M.; Tian, Z. Q. *J. Electroanal. Chem.* **1996**, *415* (1−2), 175−178.

(79) Renouprez A. J.; Jobic, H. *J. Catal.* **1988**, *113* (2), 509−516.

(80) Gordon, M. B.; Cyrot-Lackmann, F.; Desjonqueres, M. C. *Surf. Sci.* **1977**, *68*, 359−367.

(81) Hagedorn, C. J.; Weiss, M. J.; Weinberg, W. H. *Phys. Rev. B* **1999**, *60* (20), R14016−R14018.

(82) Feibelman, P. J.; Hamann, D. R. *Surf. Sci.* **1987**, *182* (3), 411−422.

(83) Oudenhuijzen, M. K.; Bitter, J. H.; Koningsberger, D. C. *J. Phys. Chem. B* **2001**, *105* (20), 4616−4622.

(84) For example, see Tables 2 and 4 in: Koningsberger, D. C.; Oudenhuijzen, M. K.; Bitter, J. H.; Ramaker, D. E. *Top. Catal.* **2000**, *10*, 167−177.

(85) Ouidenhuijzen, M. K. Thesis, University Utrecht, NL, 2002.

(86) Conway, B. E.; Angerstein-Kozlowska, H. *Acc. Chem. Res.* **1981**, *14* (2), 49−56.

(87) Freelink, T.; Visscher, W.; van Veen, J. A. R. *Electrochem. Acta* **1995**, *40* (5), 545−549 and references therein..